Optimized Substrates and Measurement Approaches for Raman Spectroscopy of Graphene Nanoribbons

Jan Overbeck,* Gabriela Borin Barin,* Colin Daniels, Mickael L. Perrin, Liangbo Liang, Oliver Braun, Rimah Darawish, Bryanna Burkhardt, Tim Dumslaff, Xiao-Ye Wang, Akimitsu Narita, Klaus Müllen, Vincent Meunier, Roman Fasel, Michel Calame, and Pascal Ruffieux*

The on-surface synthesis of graphene nanoribbons (GNRs) allows for the fabrication of atomically precise narrow GNRs. Despite their exceptional properties which can be tuned by ribbon width and edge structure, significant challenges remain for GNR processing and characterization. Herein, Raman spectroscopy is used to characterize different types of GNRs on their growth substrate and track their quality upon substrate transfer. A Raman-optimized (RO) device substrate and an optimized mapping approach are presented that allow for the acquisition of high-resolution Raman spectra, achieving enhancement factors as high as 120 with respect to signals measured on standard SiO_2/Si substrates. This approach is well suited to routinely monitor the geometry-dependent low-frequency modes of GNRs. In particular, the radial breathing-like mode (RBLM) and the shear-like mode (SLM) for 5-, 7-, and 9-atom-wide armchair GNRs (AGNRs) are tracked and their frequencies are compared with first-principles calculations.

1. Introduction

Graphene nanoribbons (GNRs)—narrow stripes of graphene—have unique electronic properties that make them an interesting material for nanoelectronic devices. In contrast to graphene, GNRs have a sizeable bandgap due to quantum confinement, which is a fundamental requirement for room temperature switching applications.[1,2] The electronic properties of GNRs can be tuned by engineering their width and edge structure.[3,4] Specifically, armchair GNRs (AGNRs) show a width-dependent electronic bandgap.[5] According to their width expressed in units of carbon atoms (N) across the ribbon, N-AGNRs can be classified into three families: $N = 3p$ (medium bandgap), $3p+1$ (wide bandgap), and $3p+2$ (quasimetallic), where p is an integer. Within each family, the bandgap scales inversely with GNR width.[6] Recent advances in the on-surface synthesis of GNRs

J. Overbeck, Dr. G. Borin Barin, Dr. M. L. Perrin, O. Braun, R. Darawish, Prof. R. Fasel, Prof. M. Calame, Dr. P. Ruffieux
Empa
Swiss Federal Laboratories for Materials Science and Technology
8600 Dübendorf, Switzerland
E-mail: jan.overbeck@empa.ch; gabriela.borin-barin@empa.ch; pascal.ruffieux@empa.ch

J. Overbeck, O. Braun, Prof. M. Calame
Department of Physics
University of Basel
4056 Basel, Switzerland

J. Overbeck, Prof. M. Calame
Swiss Nanoscience Institute
University of Basel
4056 Basel, Switzerland

C. Daniels, B. Burkhardt, Prof. V. Meunier
Department of Physics, Applied Physics, and Astronomy
Rensselaer Polytechnic Institute
Troy 12180 New York, USA

Dr. L. Liang
Center for Nanophase Materials Sciences
Oak Ridge National Laboratory
Oak Ridge, TN 37831, USA

R. Darawish, Prof. R. Fasel
Department of Chemistry and Biochemistry
University of Bern
3012 Bern, Switzerland

Dr. T. Dumslaff, Dr. X.-Y. Wang,[+] Dr. A. Narita, Prof. K. Müllen
Max Planck Institute for Polymer Research
Ackermannweg 10, 55128 Mainz, Germany

Prof. K. Müllen
Institute of Physical Chemistry
Johannes Gutenberg-Universität Mainz
55128 Mainz, Germany

have allowed to reach the required selectivity and atomic control over width and edge structure.[7,8] Scanning probe microscopy and spectroscopy studies have confirmed the intimate structure–property relationship by providing morphological and electronic information at the atomic scale.[1,4,9,10] The on-surface synthesis of atomically precise GNRs is, however, just a first step toward integrating GNRs into nanoelectronic devices which have to be followed by their controlled transfer from the metallic growth substrate (usually Au(111)) onto an insulating or semiconducting substrate appropriate for digital logic applications.[11,12] In view of device integration, this is a critical step as the quality of the GNRs needs to be preserved and thus monitored after substrate transfer. Raman spectroscopy is, so far, the only technique able to probe the structural quality of GNRs all the way from growth under ultrahigh vacuum (UHV) conditions to device integration.[5,13,14] This was demonstrated in a study reporting the first field-effect transistors (FETs) with large on/off ratio relying on 9-AGNRs as the channel material.[13] In particular, Raman spectra before and after GNR transfer were compared and the devices' high performance was directly linked to the presence of the radial breathing-like mode (RBLM) on the device. So far, however, this approach has been limited to cases with good resonance enhancement. Moreover, after transfer onto a silicon-based device substrate, most of the GNRs' low-frequency modes are hidden in the silicon background. As these low-frequency modes typically have low intensities, they require high laser powers and/or long integration times to be detected, which adversely affect the structural integrity of the GNRs.

Here, we report on the fabrication of Raman-optimized (RO) device substrates relying on the interference-based intensity enhancement provided by an amorphous dielectric layer on a metal, which blocks the background of the silicon underneath. Together with an advanced mapping approach, this results in high signal-to-noise (S/N) ratios for several excitation wavelengths while limiting radiation damage to the GNRs under investigation. Importantly, the RO layer is integrated into the device substrate itself, allowing us to systematically probe the GNRs' quality by investigating their low-frequency Raman modes. We apply this procedure to three different ribbons (5-, 7-, and 9-AGNRs) that cover all the AGNRs' families and

compare Raman spectra obtained directly on the gold growth substrate with those on the RO substrate. Finally, we discuss in detail the low-frequency modes resolved in this way and compare them with first-principles calculations.

2. Results and Discussions

Raman spectroscopy has been widely used to characterize graphite and carbon-based nanomaterials over the last five decades.[15] It is fast, potentially damage free, and particularly well suited to investigate the morphology of carbon materials at the nanoscale.[16,17] GNRs have fingerprint modes that are used to probe their quality upon growth and integration into devices.[12] The Raman spectrum of GNRs is dominated by a strong mode around $1600\,cm^{-1}$, known as the G mode, which is common to all sp^2 carbon materials and is assigned to the in-plane optical vibrations of the carbon sp^2 lattice.

The high-frequency region of the spectrum also shows modes between 1100 and $1400\,cm^{-1}$, which are a signature of the GNRs' edges. In analogy to graphene and graphite, the edges provide the necessary momentum such that the D-peak is allowed, without the need for additional disorder or defects.[18,19] The appearance of multiple peaks in this frequency range is a result of the in-plane CH-bending modes of the hydrogen-passivated edges.[20] First-principles calculations show the resulting set of edge-related normal modes[12] that we collectively refer to as CH/D modes.

The low-frequency part of the spectrum is dominated by the RBLM with a frequency that scales with ribbon width.[21,22] In addition there is the usually less intense shear-like mode (SLM) for which the atoms on the two sides of the ribbon move in opposite directions along the GNR axis,[23a] and the recently reported length-dependent Longitudinal Compressive Mode (LCM).[23b]

Figure 1 shows an overview of the fabrication and characterization process of a GNR device from UHV synthesis to the transfer onto a RO device substrate (see Experimental Section for details). GNRs are grown under UHV conditions on a vicinal Au(788) surface,[4] which promotes unidirectional growth on the narrow (111) terraces along the step edges, as shown by the scanning tunneling microscope image in Figure 1a.
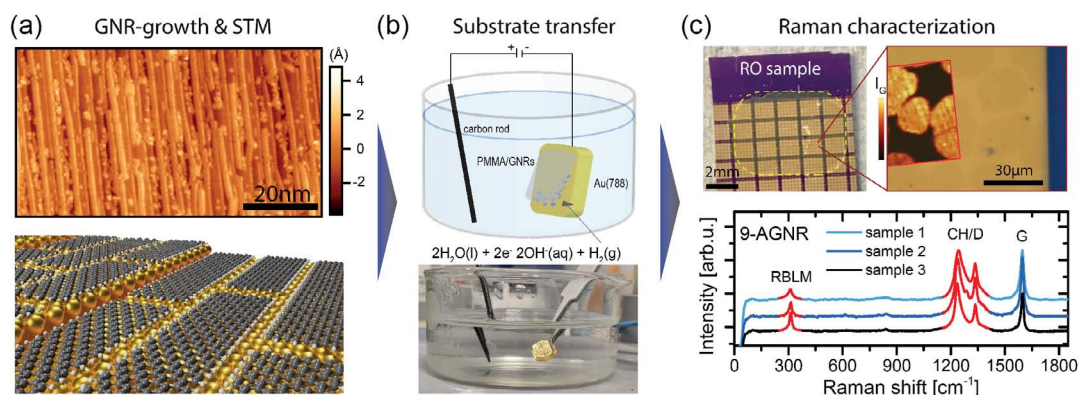

Figure 1. Sample fabrication and characterization. a) STM image of aligned 9-AGNRs (top) and a sketch of the ribbons grown parallel to the Au(788) terraces (bottom). b) Sketch of the electrochemical delamination transfer (top) and a picture of the ongoing transfer (bottom). c) Image of a RO device substrate with a transferred poly(methyl metacrylate) (PMMA)/GNR film on top (dashed outline). Optical zoom-in with Raman G-intensity map as overlay (top). Raman spectra of three different transfers illustrating the sample-to-sample variations of the RBLM, CH/D, and G modes (bottom).

Highly aligned arrays of GNRs are important to control device properties and can significantly increase device yield as well as the drain current in the transistor "on" state which is essential to meet the demands of switching applications.[24] In a second step, GNRs are transferred from the Au(788) growth substrate onto the RO substrate using an electrochemical delamination technique (Figure 1b).[25] This method preserves the uniaxial GNR alignment upon substrate transfer and thus allows for a well-defined orientation of the ribbons with respect to the device electrodes. We use Raman spectroscopy to investigate GNR quality and orientation after substrate transfer. In Figure 1c, we show an example for the characterization of the transferred GNR film. Here, the good optical contrast on the RO substrate reveals the bubble pattern of an inhomogeneously transferred film, which can be unambiguously visualized by large-area Raman mapping (overlay inset of G-peak intensity). In addition, Raman mapping shows that the peak intensity within each bubble is fairly homogeneous and that it is comparable from one bubble to the next. Consequently, spectra from within such an area can be used to characterize the transferred GNR film. In the following sections, we show Raman spectra of 9-AGNRs from different transfers. These measurements, performed on RO substrates, show significant sample-to-sample variations in the spectral regions highlighted in red. This observation underlines the importance of monitoring the GNR quality after every process step and merits further systematic investigation.

In the following, we will first discuss the mapping strategy and its benefits for the characterization of GNR samples before describing the RO substrates in more detail.

The usual approach to acquire high-quality Raman spectra is to extend the integration time. This approach, however, is problematic for GNRs because it leads to the introduction of defects by prolonged radiation exposure. The reason for this degradation of GNRs is attributed to chemical reactions activated by light (with photon energy above a certain threshold, see later). The defects, typically sp^3, are a result of photochemical reactions among the GNRs, oxygen, and ambient moisture.[25] This behavior was previously observed for graphene, in which the reaction with oxygen leads to different sp^3 defects in the basal plane and edge defects.[26,27]

In contrast, scanning a large sample area allows us to ensure that we capture the typical properties of the GNRs, exclude outliers, and get the best S/N spectra with minimal damage to the ribbons. We investigate this approach for the 5- and 9-AGNRs transferred to a RO substrate but note that this is a general observation for GNR samples. **Figure 2**a shows a time series of Raman spectra acquired on a single point of a GNR film, showing a rapidly decaying intensity (over a measurement window of 100 s). Conducted such measurements as a function of laser power (Figure 2b, top panel) shows that the damaging rate depends on light intensity. Importantly, it reveals that the damage cannot be fully avoided by reducing the laser power below a threshold. In fact, the signal intensity can be scaled to a constant power–integration time product, as shown in Figure 2b (bottom panel), indicating that the damage mechanism scales with the number of photons.

Conducting the same measurements in vacuum or with an infrared laser strongly reduces this damaging behavior as shown in Figure 2b (blue and red profiles, respectively).

Even though measuring in vacuum avoids this damaging issue, it may not be available on every experimental Raman setup and substantially increases the time necessary for investigating a sample, thereby limiting the usefulness of Raman spectroscopy to monitor device fabrication. The second approach of exclusively using infrared excitation prevents wavelength-dependent studies and is limited to Raman modes that are (near-) resonantly enhanced at these wavelengths, as nonresonant Raman is often too weak to reveal several spectroscopic features of interest in these (sub) monolayer systems. It is therefore important to limit the power–integration time product to values compatible with minimal GNR damaging.

To still achieve a good S/N ratio, we use a large-area mapping process (Figure 2c) in which a Raman map with hundreds of spectra with limited integration time is recorded. The sample is scanned at a constant speed during the acquisition of a map, such that it is displaced by typically one laser spot diameter per acquisition interval. If the integration time needed to get sufficient S/N is comparable with the previously determined timescale of ribbon damaging, the sample is scanned at a higher speed such that the radiation damage during one integration time gets spatially distributed.

While this results in decreased spatial resolution, this is usually acceptable as long as the map is restricted to a homogeneous area of the GNR film (Figure 1c).

Typically, a map of the G-peak intensity is used to check for sample homogeneity. A histogram of the peak intensity is then used to identify outliers, which are excluded if their spectra display atypical signatures that are not a simple, moderate scaling of the spectrum (Figure 2c,d). If necessary, averaging of the neighboring pixels is used to obtain a larger S/N ratio that allows to clearly identify peaks in the spectra representing a part of the scanned area. An example of this is the low-intensity peak labeled as hash (#) in Figure 2d, which could be mistaken for noise in a single spectrum. Local averaging reveals its homogeneous presence across the sample. Finally, an average spectrum is calculated from the entire homogenous sample area (excluding the mask) to give the best S/N ratio (Figure 2d).

To use Raman spectroscopy as a tool to assess GNR quality and stability, which are both critical for applications, it is desirable to perform Raman measurements directly on the final device. This is often hampered by the presence of a significant background due to the substrate (usually SiO_2/Si), which masks the GNR-related modes of interest. We show this behavior in **Figure 3**a where we compare the Raman spectra of 5-, 7-, and 9-AGNRs with that of a SiO_2/Si substrate. The Raman spectrum of silicon consists of two strong optical phonon peaks at 520 and $\approx 950\,cm^{-1}$ and an acoustic phonon peak at $300\,cm^{-1}$.[28] These three modes are in the same spectral region as the acoustic GNR modes (RBLM and SLM) that are most useful for characterizing geometry-dependent properties of GNRs. For the three different ribbons investigated in this study, we observe the RBLM at 529, 398, and $311\,cm^{-1}$ for 5-, 7-, and 9-AGNRs, respectively. In Figure 3a, we highlight in red the spectral regions for which the Si background at an excitation wavelength $\lambda_{ex} = 488\,nm$ masks the signal in a representative sample of 9-AGNRs.

To address this issue, we developed a layered, interference-optimized substrate that is suitable for both Raman and transport measurements. Interference-enhanced Raman scattering considers
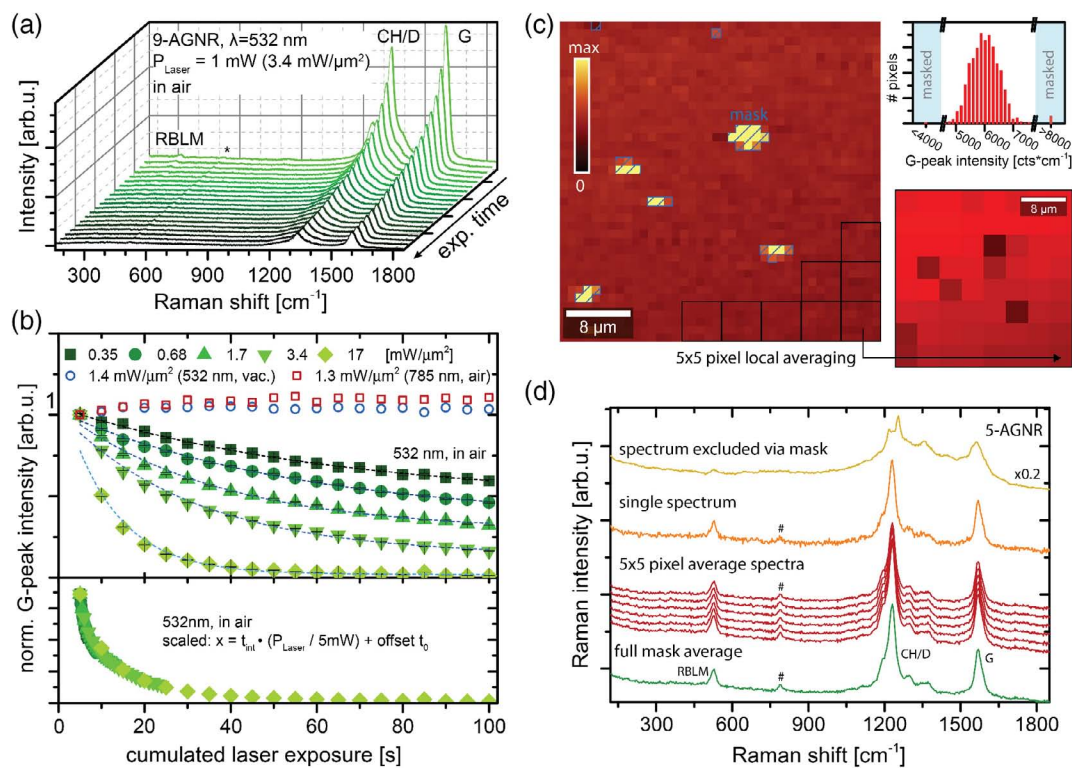
Figure 2. Laser-induced damage of GNRs and Raman mapping. a) Waterfall plot of a time series (cumulated laser exposure = 100 s) of Raman spectra on 9-AGNRs. The mode indicated by an asterisk is background from the RO substrate. 100× objective. t_{int} = 5 s. b) Top panel: G-peak intensities extracted from Lorentzian fits for several time series as a function of cumulated exposure time. The time dependence is fitted with an exponential decay for each power. For comparison, results from time series in vacuum (50× objective) and with near-infrared (NIR) excitation in air (100× objective) are shown in blue and red, respectively. Bottom panel: signal intensity scaled to a constant power–integration time product. c) Raman map with 40 × 40 pixels of 5-AGNRs on Au/mica, 50× objective, vacuum, t_{int} = 26 s. The histogram of G-peak intensities is shown in the top right and used to create a mask to exclude outliers. Local averaging is used to increase the S/N ratio and probe the homogeneity of less intense modes across the sample. d) Raman spectra from the map displayed in (c), top to bottom: impurity-dominated spectrum excluded via mask, single spectrum with S/N too low to clearly identify the mode labeled "#," local averages of 5 × 5 pixels each showing mode "#," full average over 1566 spectra in mask for the best S/N ratio.

that the layer structure of the substrate plays an important role in the measured Raman intensity, in addition to the usual factors such as set laser power, scattering cross section of the investigated material, and numerical aperture of the objective.[29] This is particularly clear for the interference of incoming and reflected laser beam that results in very different effective electromagnetic fields and therefore Raman intensities for GNRs on metallic or insulating substrates.[30] Blake et al. also reported on the optimization of substrate layer thicknesses to improve optical contrast for the fabrication of graphene-based devices by considering the light interference.[31] Interference models have further been used to describe the overall Raman intensity of thin films including graphene on oxides and explain the change in relative peak intensities as a function of oxide thickness.[30,32–35] Here, we combined these considerations to produce a substrate that is compatible with standard silicon-based fabrication approaches for nanoelectronic devices, yield good contrast for GNR film visibility, and lead to an enhanced Raman signal of GNRs without the the otherwise dominant signal of silicon as a background.

When measuring GNRs directly on a Au(788) surface or on a metallic contact pad of a device used for fabrication of

GNR-based transistors, destructive interference leads to a low electric field (and therefore low Raman scattering intensity) experienced by the GNR layer (see Supporting Information for detailed discussions and simulations). Qualitatively, one can think of the metal as a quasiperfect electric conductor that imposes an electric field node as a boundary condition. For a real metal with finite skin depth, this can be partially overcome using higher laser powers to obtain a signal at all (which in this case is possible without excessive GNR damaging). A common approach to overcome this issue is surface-enhanced Raman scattering on a nanostructured metallic substrate. In our case, however, this is not desired, as we want to assess the average properties of the GNR film and not those in plasmonic hot spots. Transferring the ribbons to a silicon substrate, instead, results in the background problems described earlier. Alternatives also include using an amorphous Raman substrate such as CaF_2, resulting in a clean, low background signal, but at the cost of severely limiting the processability for devices.

The RO structure we designed and fabricated is shown in Figure 3b and consists of an atomic layer deposition (ALD)-grown oxide layer patterned on optically thick (typically 80–90 nm) metal source-drain contacting pads (labeled S/D) on a silicon device
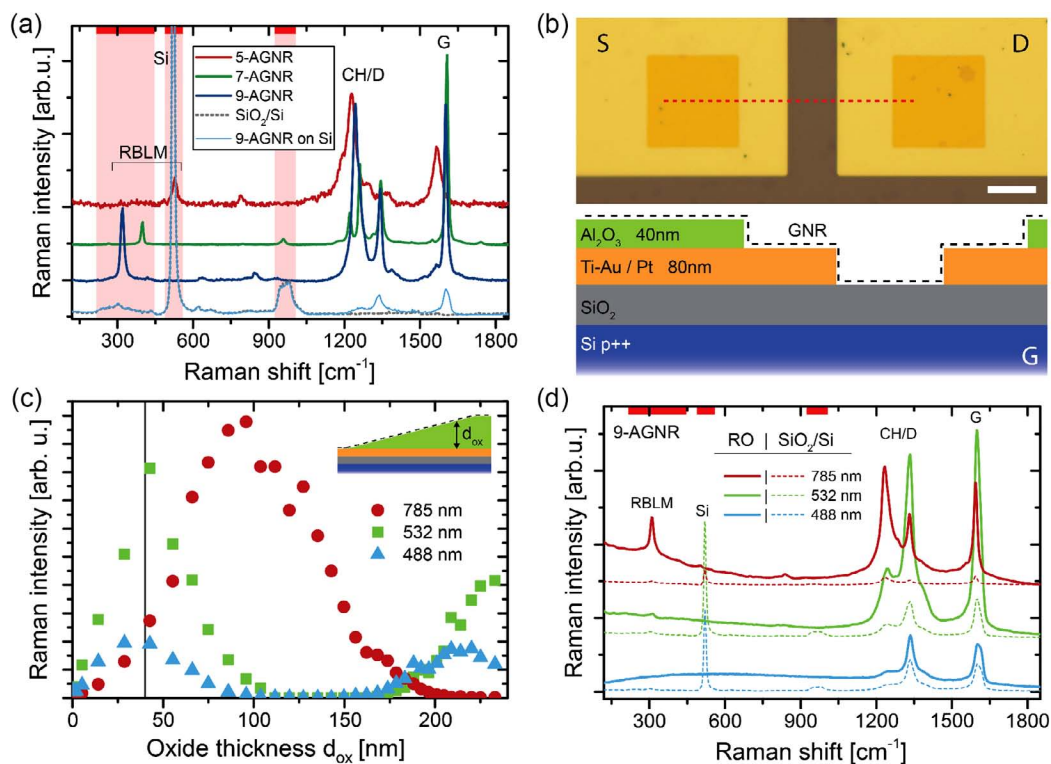
ADVANCED
SCIENCE NEWS
www.advancedsciencenews.com

pssb
physica status solidi
www.pss-b.com

Figure 3. RO device substrates. a) Raman spectra of 5-, 7-, and 9-AGNRs on Au (λ_{ex} = 785/532/785 nm, arbitrarily scaled) compared with SiO$_2$/Si and 9-AGNR transferred to SiO$_2$/Si (λ_{ex} = 488 nm), scaled to the second-order Si peak. b) Optical micrograph of an RO device substrate based on standard p-doped silicon with thermal oxide. The layers are sketched in the lower half of the panel, corresponding to the dashed red line in the optical image. c) Raman intensity of the 9-AGNR G-peak on top of an RO substrate as a function of Al$_2$O$_3$ thickness on a sample with an oxide gradient. Measured with 100× (numerical aperture (NA) = 0.9) in air. d) Raman spectra of transferred 9-AGNRs measured in the interference-optimized region (RO, solid lines) and on adjacent SiO$_2$/Si (dashed lines) with different wavelengths. Measured with 100× (NA = 0.9) in air, no background subtraction.

substrate, that acts as a support and optional gate (G). The result is enhanced optical visibility of the GNRs on top of the metal, allowing for easy identification of film inhomogeneity and a strongly enhanced Raman intensity. This is the result of the GNR layer being placed into the region of a field antinode, and it allows the acquisition of spectra at much lower excitation powers or shorter integration times.

In Figure 3c, we show the Raman intensity of the G mode as a function of oxide thickness for a 9-AGNR sample measured with three different excitation wavelengths. For each wavelength, there is an optimal thickness resulting in maximum Raman intensity (see Note 2, Supporting Information). A good compromise suitable for multiwavelength investigations of GNRs is found at an oxide thickness of about 40 nm (indicated by a vertical line), which was chosen for all subsequent studies. Figure 3d shows a comparison of the Raman spectra of 9-AGNRs transferred onto a 40 nm RO substrate and the adjacent SiO$_2$/Si substrate measured with λ_{ex} = 785, 532, and 488 nm. The spectra are shown without any background subtraction and are normalized for power and integration time. On the RO substrate, the Si background is suppressed, and an enhancement of the GNR signal by a factor of 1.5/5.3/11.7 is observed for excitation wavelengths of 488/532/785 nm, respectively. Compared with the signal directly on the Au pad, we find an enhancement of 11.5/19.5/43.0, respectively.

Note that, these values are for an oxide thickness of 40 nm, which is a compromise between the wavelengths used in this study and constraints from sample fabrication. In Figure S2, Supporting Information, we show that a substrate can be optimized for a particular wavelength of interest, by choosing an oxide thickness which satisfies the well-known condition of interference $d_{ox} \cdot n_{ox} = (2m+1) \cdot \lambda/4$, $m \in N$, where d_{ox} and n_{ox} are the thickness and the refractive index of the oxide layer, respectively.[34] In this way, one can achieve enhancement factors as high as 120 with respect to a standard SiO$_2$/Si substrate. Moreover, significant enhancement is still possible using high-quality thin gate oxides as found in state-of-the-art FETs.

To explore the benefits of our RO substrate and mapping strategy for investigating GNRs, we acquire Raman spectra with high S/N ratio for 5-, 7-, and 9-AGNRs before and after substrate transfer (**Figure 4**). The spectra acquired on the Au growth substrate are shown in black. The strong RBLM mode is visible for all three investigated ribbons. We also observe higher energy modes that are relatively clear in the case of 7-AGNRs, because this ribbon is resonant with 532 nm excitation. Similar features are much fainter for the less resonantly excited spectra of 5- and 9-AGNRs (λ_{ex} = 785 nm). The spectra after transfer are shown in red and green. The peak position and width of the intense RBLM signal have been used to monitor GNR quality and probe their stability over time.[11,12] Here, we observe several additional
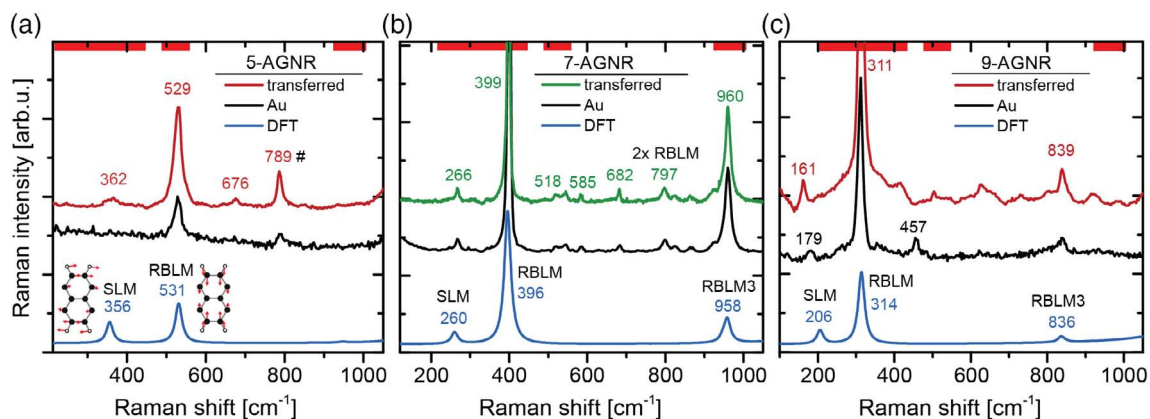
Figure 4. Raman spectra before and after substrate transfer and comparison with DFT. a) Low-energy spectrum of 5-AGNRs ($\lambda_{ex} = 785$ nm), b) 7-AGNRs (532 nm), and c) 9-AGNRs (785 nm) before and after transfer. Theoretical spectra were obtained by summing DFT-based resonant Raman intensities (all 785 nm excitation, Lorentzian line shapes with widths of 10 cm^{-1}, no frequency scaling). The most prominent peaks are labeled with position and normal mode assignment. The normal mode displacements for SLM and RBLM are exemplified for the 5-AGNR.

modes that we attribute to overtones such as the RBLM3 and higher-order processes by comparison with computed normal modes (see Note 3, Supporting Information). Most notably, for all GNRs, we observe a mode at a frequency below the RBLM. This additional fingerprint of GNRs is attributed to the SLM, which is expected to have a similar scaling with GNR width as the RBLM and has so far only been reported for 7-AGNRs.[23a] Here, we can resolve this mode for all investigated ribbons, with frequencies of about 362, 266, and 170 cm^{-1} for 5-, 7-, and 9-AGNRs, respectively.

Finally, we conducted density functional theory (DFT) calculations and computed the Raman intensities using the VASP[36–38] and Phonopy softwares.[39] The calculated spectra are shown in blue and reproduce the experimental observations well. In particular, the calculated values for the SLM frequency of 5- and 7-AGNRs closely match the experimental observations. For 9-AGNRs, there is some discrepancy with the calculations showing a mode frequency of 206 cm^{-1}, whereas experimentally, we observe it around 180 cm^{-1} on the Au growth substrate and 160 cm^{-1} after transfer (see Note 3, Supporting Information, for additional spectra). Periodic DFT, however, provides a highly idealized picture, ignoring a number of effects such as the presence of a substrate and defects in GNRs. In particular, 9-AGNRs are known to exhibit a substantial amount of phenyl defects which occur between the polymerization and the cyclodehydrogenation reaction.[9] Also, the structure of the precursor molecule for the 9-AGNRs results in slanted ribbon termini. We investigated the possibility of the edge defects or the ribbon termini causing a mode softening that could account for the difference between experimental and DFT-calculated spectra. A preliminary analysis based on calculations with the Phonopy package suggests, however, that these features alone cannot account for a mode of softening on the order of 20–40 cm^{-1}.

Finally, we note that our experimental spectra for 5-AGNRs reveal two peaks at 676 and 789 cm^{-1} that are not present in the calculated spectra. The homogeneous presence of the second peak of these modes across the sample is shown in Figure 2, and it is found for several different GNR samples (Figure S3,

Supporting Information). We find an out-of-plane mode at a calculated frequency of 784 cm^{-1} which in a strict backscattering geometry is not visible (see Figure S4, Supporting Information). Non-normal incidence from an objective with large NA or surface morphology may however relax this condition and consequently lead to the observation of additional modes.

3. Conclusions

In conclusion, we reported on the development of a RO substrate and an optimized mapping approach that allowed us to acquire detailed Raman spectroscopic information of GNRs. The RO substrates were integrated into a device-type sample geometry, which allows us to monitor the GNRs' quality during device fabrication with high S/N ratio and minimal damage to the GNRs. Finally, we investigated the GNRs' low-frequency modes, the SLM, RBLM and its overtones, and matched their frequency and mode profiles to first-principles calculations. Overall, both the RO substrate and the optimized measurement approach allowed unprecedented insight into the low-frequency modes of GNRs and demonstrated their usefulness in monitoring GNR quality upon device fabrication.

4. Experimental Section

On-Surface Synthesis of AGNRs: 9-AGNRs were synthesized from 3′,6′-diiodo-1,1′:2′,1′′-terphenyl (DITP),[40] 7-AGNRs from 10,10′-dibromo-9,9′-bianthryl (DBBA),[1] and 5-AGNRs were synthesized from an isomeric mixture of 3,9-diiodoperylene and 3,10-diiodoperylene (DIP) (details on monomer synthesis will be published in future studies) as the precursor monomers. The GNRs were grown on a vicinal single-crystal Au(788). First, Au(788) was cleaned in UHV by two sputtering/annealing cycles: 1 kV Ar$^+$ for 10 min followed by annealing at 420 °C for 10 min. In a next step, the precursor monomer was sublimed onto the Au surface from a quartz crucible heated to 70 °C (DITP) or 200 °C (DBBA and DIP), with the substrate held at room temperature. To activate the polymerization reaction, both 7- and 9-AGNRs were heated up to 200 °C (0.5 K s^{-1}) with a 10 min holding time. Subsequently, samples were

annealed at 400 °C (0.5 K s^{-1} with 10 min holding time) to form the GNRs via cyclodehydrogenation. For the synthesis of the 5-AGNRs, slow annealing (0.2 K s^{-1}) was conducted to 225 °C.

Substrate Transfer of AGNRs: AGNRs were transferred from their growth substrate Au(788) to the RO substrates by an electrochemical delamination method. First, PMMA was spin coated (2500 rpm for 90 s, four layers) on GNR/Au, to act as a support layer during the transfer, followed by a 10 min curing step at 80 °C. In a next step, the PMMA at the edges of the Au(788) crystal was removed after UV exposure (80 min) followed by 3 min development in water/isopropanol. By removing the PMMA from the crystal's edges, delamination time was reduced from 2–3 min to 45 s. The electrochemical cell was mounted using a carbon rod as the anode, the PMMA/GNRs/Au as the cathode, and 1 M NaOH as electrolyte. By applying a voltage of 5 V (current ≈0.2 A) between anode and cathode, hydrogen bubbles are formed at the interface of PMMA/GNRs and Au, resulting in the delamination of the PMMA/GNR layer. After delamination, the PMMA/GNR layer was cleaned for 5 min in purified water before being transferred to the target substrate. In the next step, the PMMA/GNRs/substrate stack was annealed for 10 min at 80 °C followed by 20 min at 110 °C to increase the adhesion between the target substrate and the PMMA/GNR layer. Finally, the PMMA was dissolved in acetone (15 min), and the final GNR/substrate rinsed with ethanol and ultrapure water.

Raman Spectroscopy: Raman spectra were acquired using a WITec Alpha 300 R confocal Raman microscope in backscattering geometry with a 50× long working distance objective (NA = 0.55, working distance = 9.1 mm), unless stated otherwise (100× objective NA = 0.9). For aligned GNRs, the linear polarization of the exciting lasers was adjusted parallel to the GNRs. The backscattered light was detected without an analyzing polarizer and coupled with one of the two spectrometers: a 300 mm lens-based spectrometer with gratings of 600 or 1800 g mm^{-1} equipped with a cooled electron multiplying charged coupled device (EM-CCD) for measurements with 488 and 532 nm excitation and a 400 mm lens-based spectrometer with gratings of 300 or 1200 g mm^{-1} and a cooled deep-depletion CCD for 785 nm excitation.

The laser wavelength, power, and integration time were optimized for each type of GNR and substrate to maximize the signal and keep the intensity loss as discussed earlier well below 10% for all settings. Unless stated otherwise, the samples were mounted in a home-built vacuum chamber at a pressure below 10^{-2} mbar, mounted on a piezo stage for scanning. A polynomial background was subtracted from the raw spectra unless otherwise stated.

First-Principle Calculations: We performed DFT calculations and calculated the Raman intensities using VASP for energy and force calculations[36–38] in conjunction with the Phonopy program package for the calculation of phonon modes and frequencies.[39] Projector-augmented wave pseudopotentials, a plane-wave cutoff of 600 eV, and the Perdew–Burke–Ernzerhof exchange–correlation functional were used in VASP. Raman intensities were calculated using in-house utility codes and the finite difference method[41] where the frequency-dependent dielectric matrix was also calculated via DFT.[42]

Supporting Information

Supporting Information is available from the Wiley Online Library or from the author.

Conflict of Interest

The authors declare no conflict of interest.

Author Contributions

J.O. and G.B.B. contributed equally to this work. J.O. and G.B.B. performed Raman measurements and data analysis, J.O. and O.B. developed and fabricated the RO devices, G.B.B and R.D. performed UHV GNR synthesis, and STM characterization and substrate transfer. T.D. and X.Y.W. synthesized the molecular precursors under the supervision of A.N. and K.M.; C.D., L.L., and B.B. performed calculations under the supervision of V.M.; G.B.B., J.O., M.L.P., R.F., and P.R. wrote the manuscript; and P.R., R.F., and M.C. initiated and supervised the project. All authors commented on the manuscript.

[1] J. Cai, P. Ruffieux, R. Jaafar, M. Bieri, T. Braun, S. Blankenburg, M. Muoth, A. P. Seitsonen, M. Saleh, X. Feng, K. Müllen, R. Fasel, *Nature* **2010**, *466*, 470.

[2] J. Cai, C. A. Pignedoli, L. Talirz, P. Ruffieux, H. Söde, L. Liang, V. Meunier, R. Berger, R. Li, X. Feng, K. Müllen, R. Fasel, *Nat. Nanotechnol.* **2014**, *9*, 896.

[3] O. Gröning, S. Wang, X. Yao, C. A. Pignedoli, G. Borin Barin, C. Daniels, A. Cupo, V. Meunier, X. Feng, A. Narita, K. Mullen, P. Ruffieux, R. Fasel, *Nature* **2018**, *560*, 209.

[4] P. Ruffieux, J. Cai, N. C. Plumb, L. Patthey, D. Prezzi, A. Ferretti, E. Molinari, X. Feng, K. Müllen, C. A. Pignedoli, R. Fasel, *ACS Nano* **2012**, *6*, 6930.

[5] L. Martini, Z. Chen, N. Mishra, G. B. Barin, P. Fantuzzi, P. Ruffieux, R. Fasel, X. Feng, A. Narita, C. Coletti, K. Müllen, A. Candini, *Carbon* **2019**, *146*, 36.

[6] Y.-W. Son, M. L. Cohen, S. G. Louie, *Phys. Rev. Lett.* **2006**, *97*, 216803.

[7] L. Talirz, P. Ruffieux, R. Fasel, *Adv. Mater.* **2016**, *28*, 6222.

[8] M. Corso, E. Carbonell-Sanromà, D. G. de Oteyza, Bottom-Up Fabrication of Atomically Precise Graphene Nanoribbons, in On-Surface Synthesis II, (Eds: D. G. de Oteyza, C. Rogero) Springer, Cham **2018**, pp. 113–152.

[9] L. Talirz, H. Söde, T. Dumslaff, S. Wang, J. R. Sanchez-Valencia, J. Liu, P. Shinde, C. A. Pignedoli, L. Liang, V. Meunier, N. C. Plumb, M. Shi,

X. Feng, A. Narita, K. Müllen, R. Fasel, P. Ruffieux, *ACS Nano* **2017**, *11*, 1380.

[10] A. Kimouche, M. M. Ervasti, R. Drost, S. Halonen, A. Harju, P. M. Joensuu, J. Sainio, P. Liljeroth, *Nat. Commun.* **2015**, *6*, 10177.

[11] A. Fairbrother, J.-R. Sanchez-Valencia, B. Lauber, I. Shorubalko, P. Ruffieux, T. Hintermann, R. Fasel, *Nanoscale* **2017**, *9*, 2785.

[12] G. B. Barin, A. Fairbrother, L. Rotach, M. Bayle, M. Paillet, L. Liang, V. Meunier, R. Hauert, T. Dumslaff, A. Narita, K. Müllen, H. Sahabudeen, R. Berger, X. Feng, R. Fasel, P. Ruffieux, *ACS Appl. Nano Mater.* **2019**, *2*, 2184.

[13] J. P. Llinas, A. Fairbrother, G. Borin Barin, W. Shi, K. Lee, S. Wu, B. Y. Choi, R. Braganza, J. Lear, N. Kau, W. Choi, C. Chen, Z. Pedramrazi, T. Dumslaff, A. Narita, X. Feng, K. Müllen, F. Fischer, A. Zettl, P. Ruffieux, E. Yablonovitch, M. Crommie, R. Fasel, J. Bokor, *Nat. Commun.* **2017**, *8*, 633.

[14] P. B. Bennett, Z. Pedramrazi, A. Madani, Y.-C. Chen, D. G. de Oteyza, C. Chen, F. R. Fischer, M. F. Crommie, J. Bokor, *Appl. Phys. Lett.* **2013**, *103*, 253114.

[15] F. Tuinstra, J. L. Koenig, *J. Chem. Phys.* **1970**, *53*, 1126.

[16] E. H. Martins Ferreira, *Phys. Rev. B* **2010**, *82*.

[17] M. S. Dresselhaus, A. Jorio, M. Hofmann, G. Dresselhaus, R. Saito, *Nano Lett.* **2010**, *10*, 751.

[18] I. A. Verzhbitskiy, M. D. Corato, A. Ruini, E. Molinari, A. Narita, Y. Hu, M. G. Schwab, M. Bruna, D. Yoon, S. Milana, X. Feng, K. Müllen, A. C. Ferrari, C. Casiraghi, D. Prezzi, *Nano Lett.* **2016**, *16*, 3442.

[19] L. G. Cançado, M. A. Pimenta, B. R. A. Neves, M. S. S. Dantas, A. Jorio, *Phys. Rev. Lett.* **2004**, *93*, 247401.

[20] R. Gillen, M. Mohr, C. Thomsen, J. Maultzsch, *Phys. Rev. B* **2009**, *80*, 155418.

[21] M. Vandescuren, P. Hermet, V. Meunier, L. Henrard, Ph Lambin, *Phys. Rev. B* **2008**, *78*, 195401.

[22] R. Gillen, M. Mohr, J. Maultzsch, *Phys. Status Solidi B* **2010**, *247*, 2941.

[23] a) C. Ma, L. Liang, Z. Xiao, A. A. Puretzky, K. Hong, W. Lu, V. Meunier, J. Bernholc, A.-P. Li, *Nano Lett.* **2017**, *17*, 6241; b) J. Overbeck, G. B. Barin, C. Daniels, M. L. Perrin, O. Braun, Q. Sun, R. Darawish, M. D. Luca, X.-Y. Wang, T. Dumslaff, A. Narita,

K. Müllen, P. Ruffieux, V. Meunier, R. Fasel, M. Calame, *ACS Nano* **2019**, https://doi.org/10.1021/acsnano.9b05817.

[24] V. Passi, A. Gahoi, B. V. Senkovskiy, D. Haberer, F. R. Fischer, A. Grüneis, M. C. Lemme, *ACS Appl. Mater. Interfaces* **2018**, *10*, 9900.

[25] B. V. Senkovskiy, M. Pfeiffer, S. K. Alavi, A. Bliesener, J. Zhu, S. Michel, A. V. Fedorov, R. German, D. Hertel, D. Haberer, L. Petaccia, F. R. Fischer, K. Meerholz, P. H. M. van Loosdrecht, K. Lindfors, A. Grüneis, *Nano Lett.* **2017**, *17*, 4029.

[26] K. P. Loh, Q. Bao, G. Eda, M. Chhowalla, *Nat. Chem.* **2010**, *2*, 1015.

[27] R. Larciprete, S. Fabris, T. Sun, P. Lacovig, A. Baraldi, S. Lizzit, *J. Am. Chem. Soc.* **2011**, *133*, 17315.

[28] P. A. Temple, C. E. Hathaway, *Phys. Rev. B* **1973**, *7*, 3685.

[29] G. a. N. Connell, R. J. Nemanich, C. C. Tsai, *Appl. Phys. Lett.* **1980**, *36*, 31.

[30] W. S. Bacsa, E. Pavlenko, V. Tishkova, *Nanomater. Nanotechnol.* **2013**, *3*, 22.

[31] P. Blake, E. W. Hill, A. H. C. Neto, K. S. Novoselov, D. Jiang, R. Yang, T. J. Booth, A. K. Geim, *Appl. Phys. Lett.* **2007**, *91*, 063124.

[32] I. H. Abidi, A. A. Cagang, A. Tyagi, M. A. Riaz, R. Wu, Q. Sun, Z. Luo, *RSC Adv.* **2016**, *6*, 7093.

[33] C. Liu, Y. Ma, W. Li, L. Dai, *Appl. Phys. Lett.* **2013**, *103*, 213103.

[34] D. Solonenko, O. D. Gordan, A. Milekhin, M. Panholzer, K. Hingerl, D. R. T. Zahn, *J. Phys. D: Appl. Phys.* **2016**, *49*, 115502.

[35] D. Yoon, *Phys. Rev. B* **2009**, *80*, 125422.

[36] G. Kresse, J. Hafner, *Phys. Rev. B* **1993**, *47*, 558.

[37] G. Kresse, J. Furthmüller, *Comput. Mater. Sci.* **1996**, *6*, 15.

[38] G. Kresse, J. Furthmüller, *Phys. Rev. B* **1996**, *54*, 11169.

[39] A. Togo, I. Tanaka, *Scr. Mater.* **2015**, *108*, 1.

[40] M. Di Giovannantonio, O. Deniz, J. I. Urgel, R. Widmer, T. Dienel, S. Stolz, C. Sánchez-Sánchez, M. Muntwiler, T. Dumslaff, R. Berger, A. Narita, X. Feng, K. Müllen, P. Ruffieux, R. Fasel, *ACS Nano* **2018**, *12*, 74.

[41] L. Liang, V. Meunier, *Nanoscale* **2014**, *6*, 5394.

[42] M. Gajdoš, K. Hummer, G. Kresse, J. Furthmüller, F. Bechstedt, *Phys. Rev. B* **2006**, *73*, 045112.

1900343 (8 of 8)